Toward Fully 3D-Printed Two Degree of Freedom Acoustic Liners

Jordan Kreitzman* and Michael G. Jones†
NASA Langley Research Center, Hampton, VA, 23681, U.S.A

An acoustic liner optimization tool is developed for designing two degree of freedom (2DOF) liners with high absorption over a wide range of frequencies and sound pressure levels (SPLs). Two additively manufactured 2DOF liners (one constant and one variable chamber depth) are designed and printed with an embedded perforate layer as the septum. A normal incidence impedance tube study is performed to directly compare impedance and absorption spectra to a more traditionally manufactured 2DOF liner with embedded mesh-caps in phenolic honeycomb. Comparisons of test data to predictions are shown as well as SPL sensitivities for each acoustic liner. Broadband absorption is achieved with the 3D-printed 2DOF liner containing constant chamber depths, although due to current limitations in printed embedded perforate hole size, not as broad as the traditional mesh-cap liner. However, results also show that the performance of the 3D-printed, variable-chamber-depth sample is closer in quality to the mesh-cap liner absorption, demonstrating the viability of printed embedded perforates in novel concepts.

I. Nomenclature

A, B, NLF	=	mesh resistance terms and the nonlinearity factor
α	=	normal incidence absorption coefficient
$\alpha_{\text{pred:m,l}}$	=	predicted absorption as a function of sound pressure level (SPL) and frequency during optimization
$\alpha_{\text{targ:m,l}}$	=	target absorption as a function of SPL and frequency during optimization
b, b_t	=	individual chamber depth and the sum of the lower and upper chamber depths
$\beta_{\text{eff}}, \beta_k$	=	admittance for the entire acoustic liner sample and for a given channel
c, ρ	=	air speed of sound and density
C_D, C_P, C_V	=	discharge coefficient and specific heat at constant pressure and volume
d, d_c	=	perforate sheet hole and chamber diameter
F	=	acoustic liner optimization tool objective function
$\gamma, \kappa, \mu, \sigma^2$	=	specific heat ratio, thermal conductivity, dynamic viscosity, and Prandtl number of air
Γ, n	=	propagation constant and value used during calculation procedure
j	=	imaginary number, $\sqrt{-1}$
$J_q()$	=	Bessel function of the first kind of order q
k, s, ω	=	free space wavenumber, shear wavenumber, and angular frequency
N_{ch}	=	number of channels in the acoustic liner system
N_f, N_{spl}	=	number of frequencies and SPLs being considered in the acoustic liner optimization tool
Ω	=	ratio of the acoustically active surface area to the total surface area of the acoustic liner
p_B	=	iterated value for acoustic pressure at the backplate, normalized by ρc^2
p_i, p_{iH}	=	acoustic pressure at i^{th} position of liner and just inside perforate hole, normalized by ρc^2
ϕ, t	=	perforate sheet open area ratio (OAR) and thickness
R	=	mesh DC flow resistance in MKS-Rayls at 1.05 m/s (41.34 in/s) acoustic particle velocity
T_{ij}	=	transmission coefficient
θ, θ_{nl}	=	acoustic liner resistance and perforate sheet nonlinear resistance, normalized by ρc
u_i, u_{iH}	=	acoustic particle velocity at i^{th} position of liner and just inside perforate hole, normalized by c
W_l, W_{spl}	=	weighting as a function of frequency and SPL used during optimization process
χ, χ_e	=	acoustic liner reactance and perforate sheet radiation reactance, normalized by ρc
ζ, ζ_c	=	acoustic liner surface impedance and the characteristic impedance term, normalized by ρc
$\zeta_{\text{eff}}, \zeta_k$	=	surface impedance for the entire acoustic liner sample and for a given channel, normalized by ρc

*Senior Research Aerospace Engineer, Structural Acoustics Branch, Research Directorate, AIAA Member.
†Senior Research Scientist, Structural Acoustics Branch, Research Directorate, AIAA Associate Fellow.

II. Introduction

Modern aircraft engine nacelles rely on two degree of freedom (2DOF) acoustic liners for broadband absorption and reduced sensitivity to the surrounding acoustic source environment. A traditional 2DOF liner is typically composed of a perforate facesheet over honeycomb chambers, where the honeycomb has either an embedded mesh or microperforate septum and a rigid backplate at the other end. Figure 1 shows a notional image of a 2DOF liner. The acoustic characteristics of a liner can be defined by its surface impedance, which is the ratio of the acoustic pressure to the acoustic particle velocity normal to the acoustic liner surface. The impedance contains both real (resistive) and imaginary (reactive) components, with contributions from the facesheet, honeycomb, and septum.

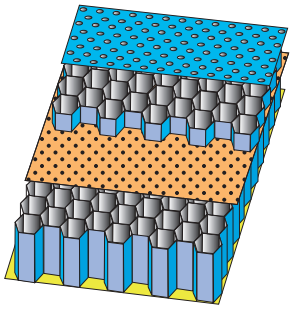

Fig. 1 Example of a two degree of freedom (2DOF) acoustic liner [Source: NASA].

As future aircraft continue to trend toward higher bypass ratio engines and shorter length nacelles for enhanced fuel efficiency, it becomes increasingly important to maximize acoustic treatment in nacelles, and even possibly on the airframe. This move toward maximizing treated area means that more complex and high curvature regions are likely to need acoustic lining. Standard manufacturing processes often have difficulties in lining areas such as these, although the industry is developing potential solutions [1]. One potential solution for these regions is the use of 3D-printing, which enables novel liner designs and chamber shapes to be implemented.

For some time, 3D-printing has been used for acoustic liner fabrication in the laboratory environment. Until recently, these designs have mostly avoided inserting septa within the chambers, as the hole sizes required for effective performance are smaller than what most 3D-printers can handle. Gautam et al. [2] explored 3D-printed liners with modular embedded septum locations, but only a single large slit was used for both the facesheet and septum. Improvements in 3D-printed processes have enabled smaller hole sizes, but these are still larger than the holes used for microperforates in traditional 2DOF liners. Regardless, there is great interest in determining the effectiveness of a fully 3D-printed 2DOF liner utilizing the current smallest available printed hole sizes. These advances give way to not only typical 2DOF printed liners, but also the potential for inserting embedded perforates within the chamber of any novel treatment being considered.

This paper focuses on three areas: (1) description of an acoustic liner optimization tool for designing 3D-printed and traditional 2DOF liners that fall within the manufacturing capabilities; (2) description of the design process, selected designs that are chosen for manufacturing and testing, and associated impedance/absorption predictions; and (3) description of the testing and results of these liners in a normal incidence impedance tube for validation of the design tool and better understanding of acoustic characteristics. It should be noted that the focus of the current effort is on developing embedded perforates to create fully 3D-printed 2DOF liners. Embedded printed meshes are also possible, albeit harder to design and print and not a focus of the current study.

III. Impedance prediction theory

The acoustic liner optimization tool used for this study is based on theory from the NASA Zwikker and Kosten Transmission Line (ZKTL) impedance prediction code [3–5], where the acoustic pressures and velocities are calculated by stepping through the acoustic liner, from the backplate to the liner surface. Figure 2 shows the computational layers for a single acoustic liner channel with an embedded perforate, where the thicknesses of the perforate sheets have been exaggerated for the clarity of the drawing. For the sake of this document, an acoustic liner channel refers to the facesheet, septum, and air chambers above and below the septum for a single unit cell of the liner.

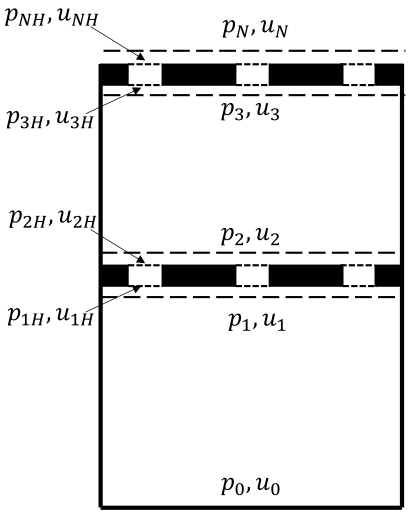

Fig. 2 Example of computational layers in the acoustic liner optimization tool.

A variety of perforate models were explored for the embedded perforate to determine which works best for the hole sizes that are of interest to this study [6–11]. This includes impedance comparisons to data derived from several sources, particularly the work included in Betts [12]. Ultimately, the wave propagation model shown in Jones et al. [13], recently assessed for accuracy in Jones et al. [14], was selected with some added modifications that will be shown in this section.

Additionally, the current code implements an iterative method at the backplate of the liner to adjust the acoustic pressure until the surface pressure matches the target sound pressure level (SPL). Therefore, this method attempts to account for the acoustic particle velocity effects not only at the facesheet but also at the embedded perforate. It is critical to properly account for the perforate sheet nonlinearities as this should be much more significant for a perforate compared to a mesh. The backplate is assumed rigid with the acoustic pressure and velocity starting value given by Eq. (1) below, where these values are normalized by ρc^2 and c, respectively.

$$\begin{pmatrix} p_0 \\ u_0 \end{pmatrix} = \begin{pmatrix} p_B \\ 0 \end{pmatrix} \tag{1}$$

The value p_B is the current iterated guess for the backplate acoustic pressure. This value will update after every iteration utilizing a simple bisection method. As shown in Fig. 2, the liner is composed of air chambers and perforate sheets. For a given air chamber, the acoustic pressure and velocity at the top of the chamber can be calculated via transmission coefficients with the acoustic pressure and velocity at the bottom of the chamber, see Eqs. (2) and (3) below.

$$\begin{pmatrix} p_{i+1} \\ u_{i+1} \end{pmatrix} = \begin{pmatrix} T_{11} & T_{12} \\ T_{21} & T_{22} \end{pmatrix} \begin{pmatrix} p_i \\ u_i \end{pmatrix} \tag{2}$$

$$T_{11} = T_{22} = \cosh(k\Gamma b); T_{12} = \zeta_c \sinh(k\Gamma b); T_{21} = \zeta_c^{-1} \sinh(k\Gamma b) \tag{3}$$

To calculate the transmission coefficients, one must first solve for the propagation constant, Γ, and characteristic impedance, ζ_c. This is done by solving for the shear wavenumber in Eq. (4), as well as the Prandtl number in Eq. (5) and the specific heat ratio in Eq. (6).

$$s = \frac{d_c}{2} \sqrt{\frac{\rho \omega}{\mu}} \tag{4}$$

$$\sigma^2 = \mu \frac{C_P}{\kappa} \tag{5}$$

$$\gamma = \frac{C_P}{C_V} \tag{6}$$

The propagation constant is then calculated using Eq. (7) below, where Eq. (8) defines the n value in the propagation constant formulation.

$$\Gamma = \sqrt{\frac{J_0(j^{3/2}s)}{J_2(j^{3/2}s)}}\sqrt{\frac{\gamma}{n}} \tag{7}$$

$$n = \left[1 + \frac{\gamma-1}{\gamma}\frac{J_2(j^{3/2}\sigma s)}{J_0(j^{3/2}\sigma s)}\right]^{-1} \tag{8}$$

Once the propagation constant is known, the characteristic impedance can be calculated via Eq. (9).

$$\zeta_c = \frac{-j}{\Gamma}\frac{J_0(j^{3/2}s)}{J_2(j^{3/2}s)} \tag{9}$$

This is the basic structure for solving the acoustic pressures and velocities within the air chamber elements of the liner. In addition to the air chambers, a very similar model can also be used to calculate the transfer impedance of an embedded perforate or top layer facesheet [13]. To do this, it is assumed that at the transition from an air chamber to a single perforate hole, continuity of acoustic pressure is maintained while the acoustic particle velocity increases due to conservation of mass. Equation (10) below shows the assumptions being made.

$$p_{iH} = p_i; u_{iH} = \frac{u_i}{\phi} \tag{10}$$

Once the acoustic pressure and velocity are defined at the entrance of a given perforate hole, Eqs. (2)–(9) can be used again to calculate the acoustic pressure and velocity at the other side of the hole, noting of course that instead of the chamber diameter, d_c, and chamber depth, b, being used, the perforate sheet hole diameter, d, and sheet thickness, t, are used. Once the acoustic pressure and velocity are defined at the other end of the perforate hole, similar logic as Eq. (10) can be applied for the acoustic pressures and velocities just above the holes. Equation (11) below shows this.

$$p_{i+1} = p_{(i+1)H}; u_{i+1} = u_{(i+1)H}\phi \tag{11}$$

There are additional assumptions that can be made to further modify Eq. (11). For one, this method for calculating the impedance does not capture the nonlinear resistance of a perforate caused by the turbulent mixing loss of the acoustic waves exiting the holes. Equation (12) can be used to account for this [8, 15].

$$\theta_{nl} = \frac{(1-\phi^2)}{2\phi^2 C_D^2}|u_{i+1}| \tag{12}$$

Additionally, since this model is only properly accounting for acoustic behavior inside the holes, it also neglects the radiation impedance effects, typically applied as a mass end correction term in the reactance, shown as Eq. (13) below [6, 16].

$$\chi_e = 0.85kd\frac{1-0.7\sqrt{\phi}}{\phi} \tag{13}$$

Equation (11) for the acoustic pressure can be modified with Eqs. (12)– (13) to represent an additional acoustic pressure change associated with the nonlinear resistance and radiation reactance, shown below as Eq. (14). Note that an assumption of the perforate sheet being a lumped element (i.e., no change of particle velocity across the sheet) is assumed for these added terms. For the sheets that are being considered in this study, this is a reasonable assumption.

$$p_{i+1} = p_{(i+1)H} + (\theta_{nl} + j\chi_e)u_{i+1} \tag{14}$$

An additional consideration is added for looking at cases of a more traditional 2DOF acoustic liner, which contains embedded mesh-caps instead of a perforate. For this case, the mesh is assumed very thin so that the reactance effects are negligible and only resistive effects are applicable. Equation (2) can be used again, except this time Eqs. (15) and (16) define the transmission coefficients. Here it is assumed that the resistance of the mesh is defined at 1.05 m/s (41.34 in/s) particle velocity (industry standard) and that the mesh has minor nonlinear effects on the resistance.

$$T_{11} = T_{22} = 1; T_{12} = A + B|u_i|; T_{21} = 0 \tag{15}$$

$$B = (\mathrm{NLF} - 1)\frac{\mathrm{R}}{\rho \mathrm{c}(\frac{0.95}{\mathrm{c}} + \mathrm{NLF}\frac{0.85}{\mathrm{c}})}; \mathrm{A} = \frac{\mathrm{R}}{\rho \mathrm{c}} - \mathrm{B}\frac{1.05}{\mathrm{c}} \tag{16}$$

For acoustic liners that vary in impedance across the face of the sample (e.g., variable-chamber-depth liners), one can compute an effective impedance. To do this, the normalized surface impedance of a single channel is defined in Eq. (17), where the impedance is the ratio of the normalized acoustic pressure to acoustic particle velocity. The admittance is then the reciprocal of this value.

$$\zeta_k = \frac{p_n}{u_n}; \beta_k = \frac{1}{\zeta_k} \tag{17}$$

The effective admittance of the entire liner can then be calculated as a weighted summation of the admittances of each channel, and the reciprocal can be taken to find the effective impedance of the liner system, see Eq. (18) below.

$$\beta_{\mathrm{eff}} = \frac{\Omega}{N_{\mathrm{ch}}} \sum_{k=1}^{N_{\mathrm{ch}}} \beta_k; \zeta_{\mathrm{eff}} = \frac{1}{\beta_{\mathrm{eff}}} \tag{18}$$

Please note that the impedance prediction process shown in this section is for a single frequency and must be repeated for every frequency of interest.

IV. Acoustic liner optimization process

The impedance modeling approach described above was implemented in a set of Python scripts and coupled with a nonlinear optimization routine, NLopt [17]. Specifically, the BOBYQA [18] algorithm was implemented, which is a derivative free bound constrained local minimum solver. Many geometric parameters can be optimized in this process, although it should be noted that because it solves for a local minimum and not a global minimum, the optimized design output has some dependency on the starting guess. Table 1 shows the geometric parameters and ranges that were considered during the design process for the 3D-printed and traditional 2DOF constant-chamber-depth liners. The "Embedded septum height" refers to the distance between the septum and the backplate as a ratio of the total chamber depth, b_t. It should also be noted that b_t is the sum of the lower and upper chamber depths and does not include the thickness of the embedded perforate or facesheet. Additionally, discharge coefficients, C_D, were assumed for the facesheet and embedded perforate with values that were similar to data available for perforates of comparable geometry.

Table 1 Acoustic liner geometric parameters and ranges for 2DOF constant-chamber-depth liner optimization.

Geometric parameters	3D-Printed 2DOF	Traditional 2DOF
b_t	0.300"–2.000"	0.375"–2.000"
Embedded septum height	$0.1b_t$–$0.9b_t$	$0.1b_t$–$0.9b_t$
Facesheet ϕ	0.04–0.16	0.04–0.16
Facesheet t	0.03"–0.06"	0.03"–0.06"
Facesheet d	0.03"–0.06"	0.03"–0.06"
Facesheet C_D	0.85	0.85
Embedded perforate ϕ	0.01–0.08	N/A
Embedded perforate t	0.016"–0.040"	N/A
Embedded perforate d	0.005", 0.015", 0.020"	N/A
Embedded perforate C_D	0.90	N/A
Embedded mesh-cap R	N/A	200–1400 MKS-Rayls
Embedded mesh-cap NLF	N/A	1.75
Ω	0.5625	1.0000

A high-resolution printer using stereolithography (SLA) at a commercial 3D-printing facility was used to print the 2DOF liner samples. Hole diameter accuracy for the printer is quoted as 0.020", although some early test prints showed

that hole diameters down to 0.015" were resolved, albeit at the expense of inconsistent hole sizes [19]. It was found early on that the optimizer always pushed for the smallest embedded perforate hole diameter to maximize performance. Therefore, a range for the diameters during the optimization process was not needed. Rather, three hole diameters were selected in order to understand the improvements in design that could be obtained as one goes down in hole size, noting of course that 0.005" hole diameter is not currently possible to manufacture using the available 3D-printer.

For the purposes of preliminary design in the normal incidence impedance tube, all liners targeted an absorption coefficient of 1.0 for a broadband frequency range of 1,000 Hz – 5,000 Hz in 200 Hz increments. Additionally, SPL values of 120, 130, 140, and 150 dB were considered during the optimization. These frequencies and SPLs were chosen based on typical acoustic environments to which these liners would be exposed for a typical aircraft nacelle. Normal incidence absorption coefficients (α) were calculated using Eq. (19) below utilizing the resistance (θ) and reactance (χ) terms of the impedance (ζ) output from the optimizer code.

$$\alpha = \frac{4\theta}{(1+\theta)^2 + \chi^2}; \zeta = \theta + j\chi \tag{19}$$

The objective function for optimization (minimization in this case) was the difference between the targeted and predicted absorption coefficient. This is shown numerically as Eq. (20) below, where for the purposes of this paper, every frequency and SPL of interest was weighted the same. It should be noted that although the absorption coefficient is 1.0 when the impedance is 1+0j, the objective function is not targeting 1+0j impedance. This process would weight the resistance and reactance equally. By specifically targeting absorption coefficient instead, the resistance and reactance are weighted differently. Some preliminary optimization exercises indicated that one will get different designs depending on these differences in objective functions. It is also important to note that the total chamber depth for each liner was allowed to vary, i.e., liners were not compared on an equivalent chamber depth basis.

$$F = \sum_{m=1}^{N_{\text{spl}}} W_m \sum_{l=1}^{N_f} W_l |\alpha_{\text{targ:m,l}} - \alpha_{\text{pred:m,l}}| \tag{20}$$

The results from the optimizer are shown in Table 2 for both the 3D-printed (P1–P3) and traditional mesh-cap (T1) 2DOF acoustic liners. Note that three different embedded perforate hole diameters were assessed to understand the trend in absorption improvement for the 3D-printed liners. Additionally, "Total channel height" in Table 2 refers to the summation of the upper and lower chamber depths (b_t) as well as the septum and facesheet thicknesses, where the mesh-caps are assumed to have negligible thickness.

Table 2 2DOF constant-chamber-depth optimized liner designs.

Geometric parameters	P1	P2	P3	T1
Facesheet ϕ	0.1600	0.1405	0.1296	0.1309
Facesheet t	0.0300"	0.0300"	0.0300"	0.0389"
Facesheet d	0.0300"	0.0300"	0.0300"	0.0300"
Embedded septum height	0.7484"	0.4940"	0.4362"	1.1408"
Total channel height	1.5060"	1.1993"	1.1213"	1.6202"
Embedded perforate ϕ	0.0764	0.0220	0.0211	N/A
Embedded perforate t	0.0398"	0.0160"	0.0160"	N/A
Embedded mesh-cap R	N/A	N/A	N/A	900.6146 MKS-Rayls
Embedded perforate d	**0.0050"**	**0.0150"**	**0.0200"**	N/A

Figure 3 shows the predicted absorption curves for the three 3D-printed designs in Table 2 from 600 to 6,000 Hz at tonal source inputs of 120, 130, 140, and 150 dB. As expected, it is evident that the 0.005" hole diameter design (P1–shown as orange triangles) is best, particularly considering the low dependence on SPL. This is advantageous in that the acoustic liner will perform similarly under a wider array of acoustic environments. There is a sizable improvement from 0.015" (P2–shown as green triangles) to 0.005" (P1). However, the predicted improvement from 0.020" (P3–shown as pink squares) to 0.015" (P2) is minimal. Coupled with the fact that the 0.015" targeted holes are difficult to manufacture properly, it was decided to focus on the 0.020" hole diameter design (P3) going forward for

the embedded perforate. This ensured higher accuracy in the printed design while theoretically suffering only minor penalties in the absorption quality.

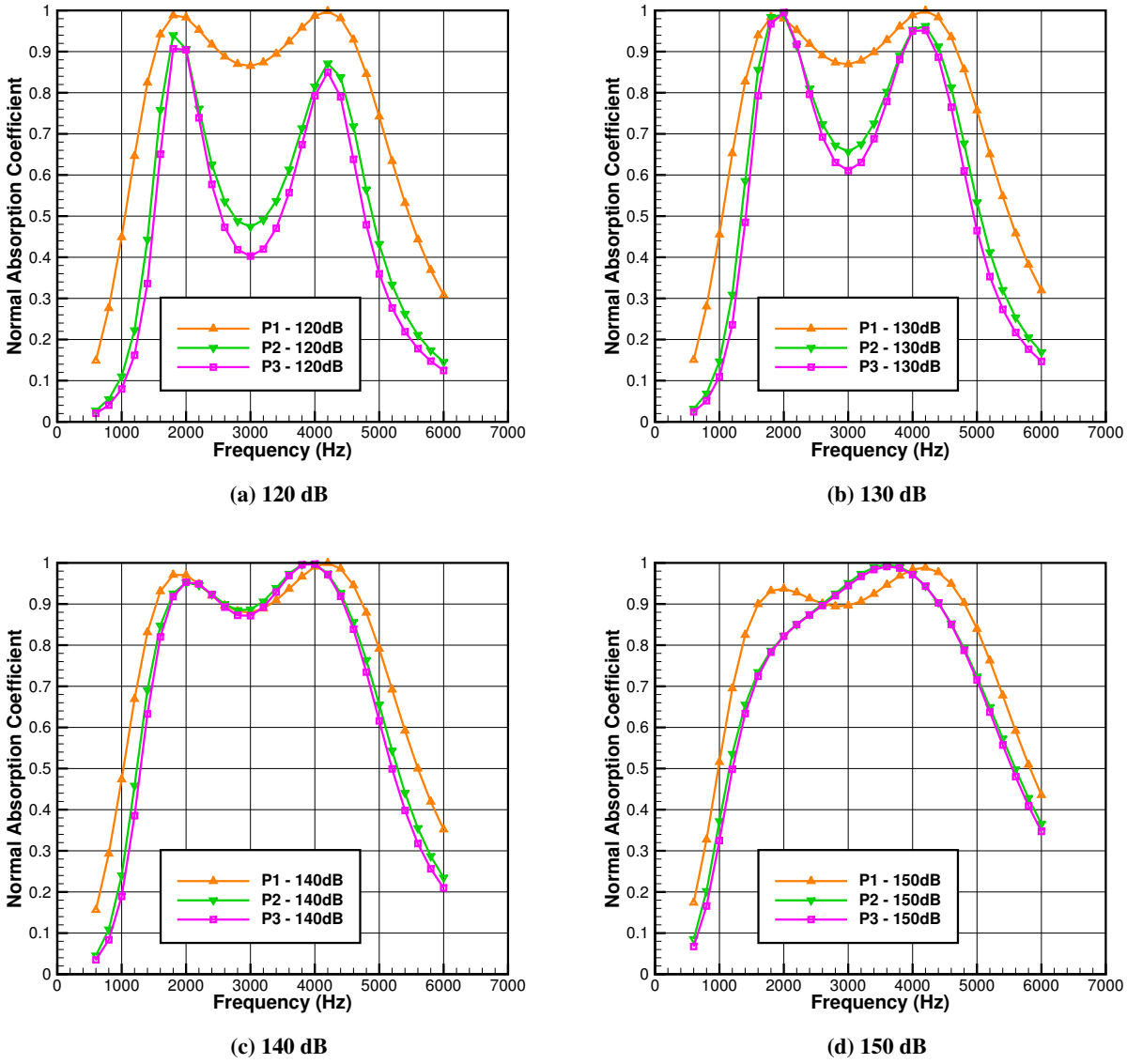

Fig. 3 Normal incidence absorption coefficient vs. frequency (Hz) for P1, P2, and P3 optimized designs at SPL values of 120, 130, 140, and 150 dB.

After finalizing the 0.020" hole diameter for the 3D-printed, constant-chamber-depth design, the variable-chamber-depth design was then explored. It was decided to focus on two variable channels for the design, where the acoustic liner is a repeating pattern of these two channels, defined as channels 1 and 2. The location and geometry of the embedded perforates were allowed to vary between channels 1 and 2, except of course for the hole diameter where 0.020" was chosen for both. The same parameters used for optimization with the 3D printed constant-chamber-depth samples (shown in Table 1) were also used for channels 1 and 2 in the variable-depth sample. The facesheet, however, was designated to be the same over channels 1 and 2. The optimized design for the 2DOF variable-chamber-depth liner is shown in Table 3 as P4. Note that for this design, more of the available total chamber depth is utilized.

Table 3 2DOF variable-chamber-depth optimized liner design – P4.

Geometric parameters	Channel 1	Channel 2
Facesheet ϕ	0.1600	0.1600
Facesheet t	0.0300"	0.0300"
Facesheet d	0.0300"	0.0300"
Embedded perforate height	0.7796"	0.3196"
Total channel height	1.9189"	0.9449"
Embedded perforate ϕ	0.0274	0.0178
Embedded perforate t	0.0160"	0.0160"
Embedded perforate d	**0.0200"**	**0.0200"**

V. Acoustic liner designs

A. 3D-printed designs

Once the optimum liner designs were determined, the configurations were adapted for normal incidence impedance tube testing. The P3 and P4 acoustic liners can be seen in Fig. 4. These samples consist of a 5x5 array of 0.3"x0.3" square cross-section chambers and 0.1" partition thicknesses. The facesheet and chambers are printed as one integrated piece so as to improve structural rigidity of the samples. The bottom of the lower chambers is left open to allow the resin from the SLA printing process to drain out. During impedance testing, the samples are rested on a flat metal plate to act as the rigid backplate.

Figure 4 shows the additional design considerations needed for the P4 liner. Because the P4 liner is a variable-chamber-depth liner with two repeating patterns, one channel is longer than the other. This means that for the shorter channel, a backplate is integrated into the design. Because the resin needs to drain out of the chamber, the backplate has a tapered hole (0.10" diameter going down to 0.05"). During the post-processing of the sample, this tapered hole is then sealed with Bondo Spot putty. Since the sample itself has the thickness of the longer channel, there is an air chamber below the small channel backplate that is unused.

During the optimization process, the open area ratios (OARs) of the liners were not directly coupled to the hole count. In other words, the program did not take into account that certain OAR values are not possible given the hole diameter and an integer number of holes. Therefore, the OAR was adjusted to the closest possible value utilizing an integer number of holes. The OAR itself is computed based on the number of holes per chamber, not the number of holes over the entire facesheet.

In addition to the change in OAR, the printing process itself contains tolerances. Quality assurance was performed on the P3 and P4 liners post-print to measure the actual hole diameters. Since the liners were printed as one integrated piece, other characteristics of the liner could not be measured easily, so for the quality assurance, only the facesheet and septum hole diameters were measured. For the P4 liner, the septum within the smaller channel could not be assessed due to the integrated backplate impeding access. The actual geometric parameters for the P3 and P4 liner samples used for the predictions to the test data are shown in Table 4. Note that the septum hole diameters printed out a bit larger than they should have for the P4 liner, and this of course then also raised the septum OAR, thereby degrading the performance a bit. Additionally, it should be pointed out that "P4(1)" and "P4(2)" in Table 4 is referencing channels 1 and 2 respectively for the P4 acoustic liner.

B. Traditional mesh-cap design

For the traditional mesh-cap liner (T1), the total chamber depth needed to be slightly lowered to 1.5", and there were tolerances during manufacturing associated with the mesh-cap insertion depth, resistance, and nonlinearity factor. The honeycomb with inserted mesh-caps was manufactured by the Hexcel Corporation under a Space Act Agreement (SAA1-33328). A facesheet was 3D-printed and press fit over the honeycomb chambers. The facesheet along with the honeycomb is shown in Fig. 4. It is important to point out that for the P3 and P4 liners, the facesheets were specifically designed to maintain OAR over each chamber separately. For the T1 mesh-cap liner, since the honeycomb chamber walls are assumed to be of negligible thickness, the facesheet was designed to be entirely uniform across the entire facesheet face. The geometric parameters of the final acoustic liner sample (T1) are shown in Table 4. Note that the

Table 4 2DOF liner actual geometric parameters.

Geometric parameters	P3	P4(1)	P4(2)	T1
Facesheet ϕ	0.1174	0.1677	0.1677	0.1204
Facesheet t	0.0300"	0.0300"	0.0300"	0.0410"
Facesheet d	0.0290"	0.0310"	0.0310"	0.0290"
Embedded septum height	0.4362"	0.7796"	0.3196"	1.0670"
Total channel height	1.1213"	1.9189"	0.9449"	1.5410"
Embedded perforate ϕ	0.0209	0.0338	0.0211	N/A
Embedded perforate t	0.0160"	0.0160"	0.0160"	N/A
Embedded mesh-cap R	N/A	N/A	N/A	934.5000 MKS-Rayls
Embedded perforate d	**0.0200"**	**0.0220"**	**0.0220"**	N/A
Embedded mesh-cap NLF	N/A	N/A	N/A	1.5850

nonlinearity and resistance came out a bit different than what was originally intended.

VI. Test facilities background and description of test

Two impedance tubes are used for testing: the NASA Langley Normal Incidence Tube (NIT) and High Intensity Modal Impedance Tube (HIMIT). Figure 5 shows schematics of each. The HIMIT is a new rig in the Liner Technology Facility at NASA Langley, designed to evaluate acoustic liners at SPLs up to 170 dB and frequencies up to 6 kHz in no flow. It is a 2" x 2" waveguide of approximately 14" in length, where the sound can be injected into the tube in one of two ways: either through two compression drivers or a Hartmann generator. A 0.25" diameter reference microphone is mounted 0.25" from the liner surface to determine the total SPL at the acoustic liner surface when tests are conducted at frequencies where the sound field is confined to plane waves. Eight 0.125" diameter measurement microphones are mounted in four rotating plugs with two on the upper wall and two on the right wall. This unique microphone setup is needed to perform the modal decomposition necessary for higher order modes present at higher frequencies in the duct, where the power distribution and propagation constants of each mode are identified. It should be noted that the measurement microphone positions for the HIMIT shown in Fig. 5 are changed to positions more ideal for the modal decomposition process. These eight microphones and modal decomposition approach are also required to correctly set the SPL at the acoustic liner surface when tests are conducted at higher frequencies resulting in higher order modes [20, 21].

Currently, the 0.25" reference microphone is used to set the total SPL for all frequencies, which is not quite accurate for the higher frequencies where higher order modes are present. This process will be changed in the near future. The mode with the highest incident power for the desired frequency is used to determine the liner impedance more accurately [20, 21]. Currently, only a stepped sine tonal source can be utilized in the HIMIT, so this rig is currently limited in its frequency resolution [22].

The NIT is a 2" x 2" waveguide of approximately 36" in length. It uses six 120 W compression acoustic drivers to generate a sound field that impinges on the acoustic liner surface. There are 3 flush-mounted microphones associated with the rig. One is a reference microphone 0.25" away from the sample surface and is used to help achieve the appropriate SPL for the test. Two other microphones are then placed 2.50" and 3.75" from the liner surface and are mounted in a rotating plug so that their positions can be interchanged. This allows errors associated with the amplitudes and phases due to mismatched microphone calibrations to be eliminated during the two-microphone method process. The NIT allows for 3 different source types: stepped sine, swept sine, and broadband. For this particular study, swept sine will be used, which is a controlled amplitude swept sine source that can maintain ±0.5 dB amplitude accuracy with approximately 5 Hz resolution [22].

As shown above, the HIMIT can output data to higher frequencies and SPLs. The NIT is needed for this study for two particular reasons. One, since the HIMIT is a new test rig, the NIT is being applied to verify results, at least within the frequency range that the NIT operates. Additionally, the swept sine source of the NIT allows for enhanced frequency resolution that cannot currently be obtained with the HIMIT. These two test rigs are used together to get a more complete picture of each sample. Table 5 shows the test matrix that was used for the T1, P3, and P4 liner samples.

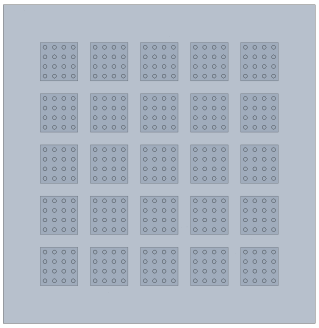

(a) P3 top view

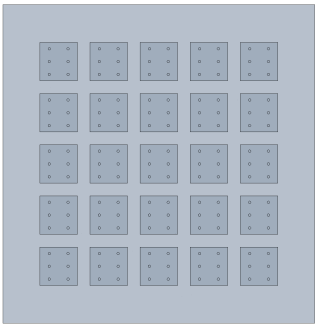

(b) P3 bottom view

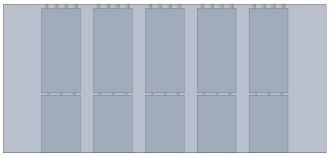

(c) P3 side view

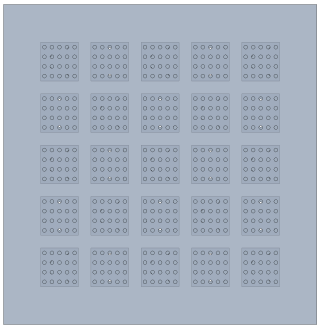

(d) P4 top view

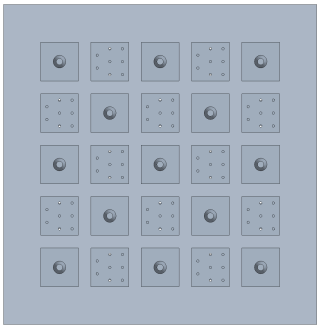

(e) P4 bottom view

(f) P4 side view

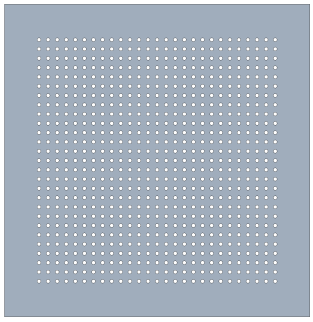

(g) T1 facesheet

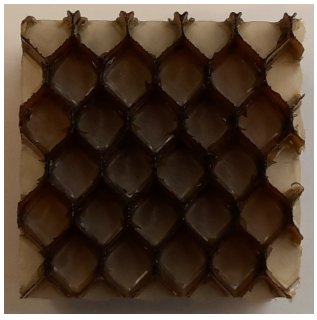

(h) T1 top view

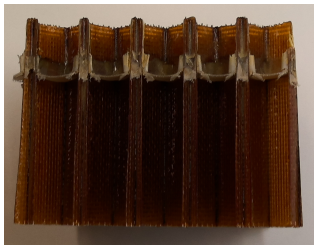

(i) T1 side view

Fig. 4 Acoustic liner designs.

Note that the NIT is only used for SPL values of 120 and 140 dB, whereas the HIMIT also includes 130 and 150 dB.

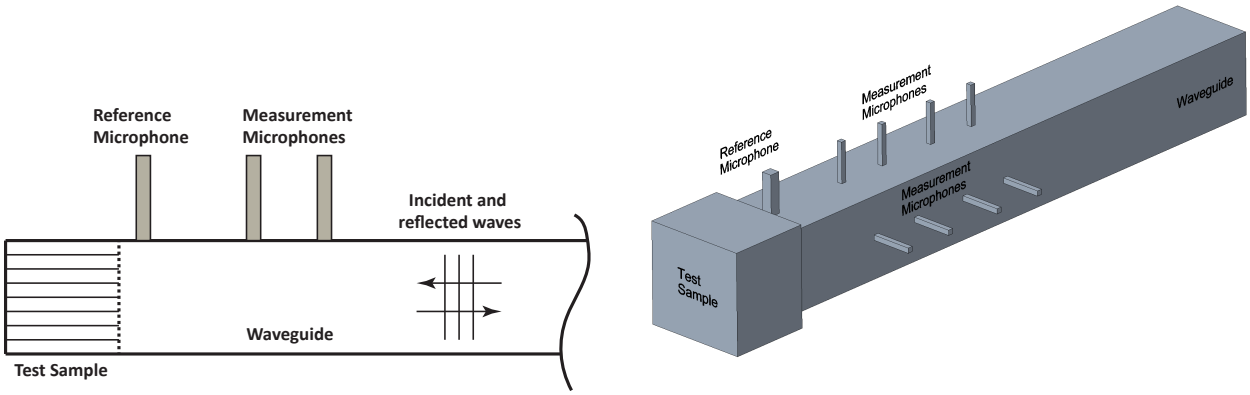

(a) Normal Incidence Tube (NIT). **(b) High Intensity Modal Impedance Tube (HIMIT).**

Fig. 5 Impedance tube test rigs [Source: NASA].

Table 5 Impedance tube test matrix.

Sample Descriptor	Test Rig	Source Type	SPL	Frequency Range
T1	NIT	Swept Sine	120, 140 dB	400Hz–3000Hz, Δf = ~5Hz
T1	HIMIT	Stepped Sine	120, 130, 140, 150 dB	600Hz–6000Hz, Δf = 200Hz
P3	NIT	Swept Sine	120, 140 dB	400Hz–3000Hz, Δf = ~5Hz
P3	HIMIT	Stepped Sine	120, 130, 140, 150 dB	600Hz–6000Hz, Δf = 200Hz
P4	NIT	Swept Sine	120, 140 dB	400Hz–3000Hz, Δf = ~5Hz
P4	HIMIT	Stepped Sine	120, 130, 140, 150 dB	600Hz–6000Hz, Δf = 200Hz

VII. Test results and comparison to predictions

The normalized impedance for the P3, P4, and T1 acoustic liners at 120 and 140 dB taken in the NIT and HIMIT are shown in Figs. 6, 7, and 8. Good agreement is seen between the NIT and HIMIT data within the frequency range of the NIT's capabilities (up to 3,000 Hz), although discrepancies do exist. Some of these differences can be attributed to slightly different characteristic air impedances during tests. Since these tests were not all run on the same day, ambient air static pressures and temperatures varied slightly from day to day. Other differences could exist due to the different methods being used for impedance extraction, as the NIT is using the two-microphone method while the HIMIT must use a modal decomposition technique with eight measurement microphones. There are also possible anomalies in the higher frequency data for HIMIT. This includes the assumption of highest incident power mode being used to determine the impedance, as well as anomalies existing when new modes are first cut-on in the duct. All things considered, fairly good agreement in test data between the two rigs is seen for all three liners, although it appears that the greatest discrepancy exists for the T1 liner, which could be attributed to the press fit of the facesheet over the honeycomb and the two different holders used for the honeycomb during the tests.

In terms of the predictions, it is important to note that there was a change made in the radiation impedance term (Eq. (13)) for comparisons to the normal incidence data, as the hole interaction effect should be modified slightly for a purely normal incidence environment [16]. This slight correction was added to all predictions documented in this paper

and shown below as Eq. 21.

$$\chi_e = 0.85kd\frac{1 - 1.25\sqrt{\phi}}{\phi} \tag{21}$$

It can be seen in Figs. 6, 7, and 8 that the predictions typically agree quite well with the impedance data over a wide range of frequencies. This validates the optimization process used to design the acoustic liners, although it should be noted that improvements can certainly be made to the prediction process, particularly at 140 dB. This is not a surprise, as it is well known that higher SPLs tend to reduce the mass end correction values, thereby altering the radiation impedance and shifting the reactance curves down [15]. This effect is not currently accounted for in the design code. Additionally, it is important to point out that the SPL used in the prediction process is based on the reference microphone measurement. At higher frequencies where higher order modes exist, the SPL across the liner face will vary. Future predictions should utilize the data from the measurement microphones to use an averaged SPL over the liner face. This may also explain some discrepancies between prediction and test at higher frequencies.

One can see the SPL sensitivity of the P3 acoustic liner in Fig. 6, as the impedance varies greatly between 120 and 140 dB. As mentioned earlier, the designs were targeting an absorption coefficient of 1.0 from 1 to 5 kHz, which correlates to a 1+0j impedance. The P3 reactance at 120 dB does not appear to hold near zero particularly well, as its reactance curve actually more closely resembles that of a single degree of freedom liner, albeit its antiresonance is not as severe. It relies on the SPL of the incoming acoustic source (and hence the acoustic particle velocity) to provide sufficient resistance and broaden the reactance curve near zero. This is in direct contrast to the T1 acoustic liner, as Fig. 8 shows how insensitive the liner is to SPL due to the use of embedded mesh-caps being driven by viscous loss resistance.

Figure 9 shows normal incidence absorption coefficients for all three liners at 120, 130, 140, and 150 dB, including the predictions. Note that the NIT data only exist for 120 and 140 dB. The results obtained in the NIT compare favorably with those obtained in the HIMIT. Predicted absorption curves also tend to agree very well with the test data.

The normal incidence absorption coefficients of all acoustic liners together are shown in Fig. 10. By analyzing Fig. 10, it becomes clear that the T1 embedded mesh-cap acoustic liner outperforms both the P3 and P4 liners over the 1-5 kHz targeted range and all targeted SPLs. This was an expected finding, and the T1 liner also remains consistent across all SPLs due to its linear mesh. The P3 liner fails to be as consistent across the SPL range due to the embedded perforate's highly dependent nature on acoustic particle velocity and hence SPL. Reduced performance at 120 and 130 dB was offset by increased performance at 140 and 150 dB during the design optimization process. Of course, a lower OAR used for the P3 liner could have resulted in improved performance at 120 and 130 dB, but the intent of the design was to try and maximize performance across a wide range of SPLs. All in all, the P3 liner fails to provide the same absorption performance as the T1 liner across every SPL, particularly at the lower frequencies. Part of this is due to the difference in chamber depth between the two (P3 liner has a smaller depth), but simply forcing the P3 liner to maximize chamber depth would subsequently degrade the higher frequency performance. This trade was assessed during the design phase. By studying Fig. 10 as well as Fig. 3, it would appear that a 0.020" hole diameter is simply not small enough for the embedded perforate to provide performance similar to the T1 liner, although it still provides broadband absorptive performance that exceeds that of basic single degree of freedom liners. As 3D-printers advance and are able to print out smaller holes, it will improve the linearity of the 2DOF liner and better approach that of a typical mesh-cap liner.

Variable-chamber-depth lining helps mitigate the impact of having to use larger holes associated with the embedded perforates. The P4 liner data in Fig. 10 shows improved performance compared to the P3 liner. While not as good as the T1 liner, its absorption performance is in between that of P3 and T1, including lowered SPL sensitivity compared to P3. One can envision that since this was only a variable-chamber-depth pattern of two, adding more degrees of freedom to this design would further improve performance and approach that of the T1 liner. One can expand on this idea as well to include things such as variable-depth, bent-chamber liners with embedded perforates and other 3D-printed novel concepts.

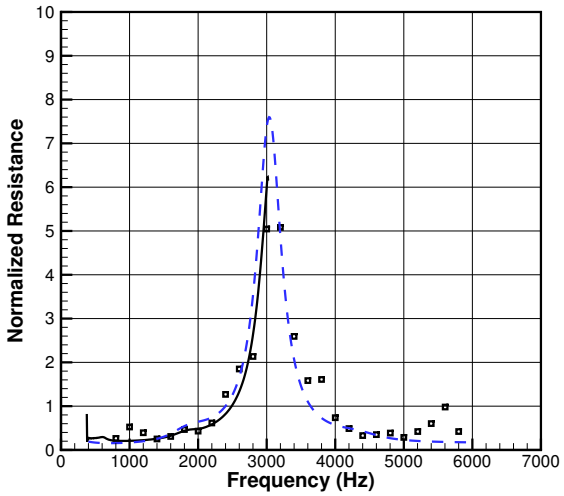

(a) 120 dB resistance

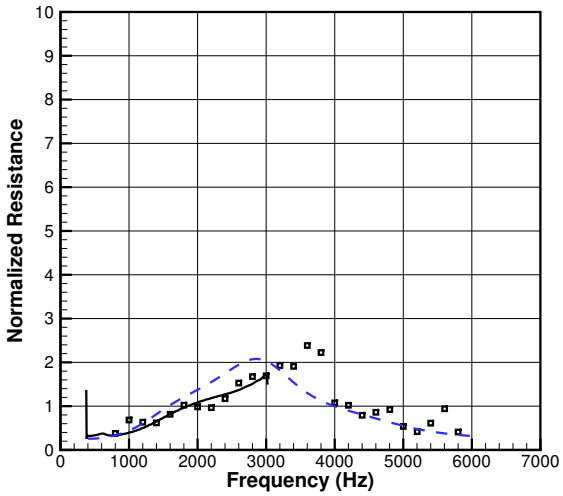

(b) 140 dB resistance

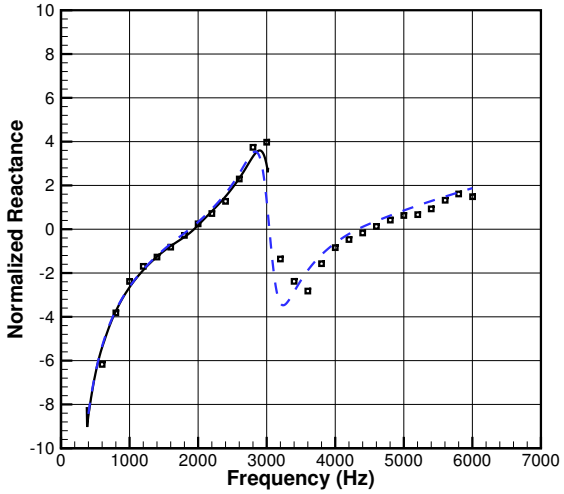

(c) 120 dB reactance

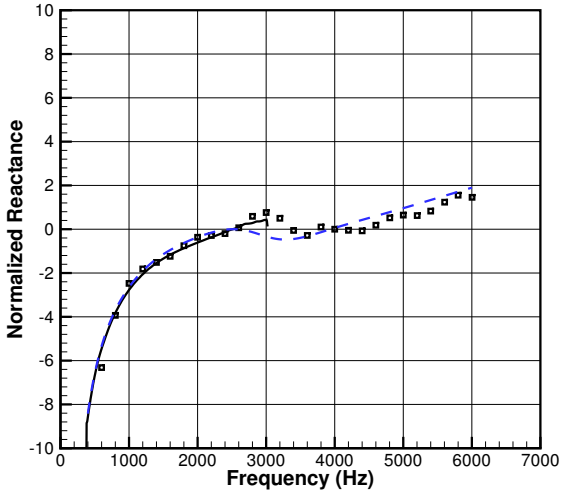

(d) 140 dB reactance

Fig. 6 Normalized impedance vs. frequency (Hz) for the P3 sample at SPL values of 120 and 140 dB. Black line is NIT data; Black squares are HIMIT data; Blue dashed line is prediction.

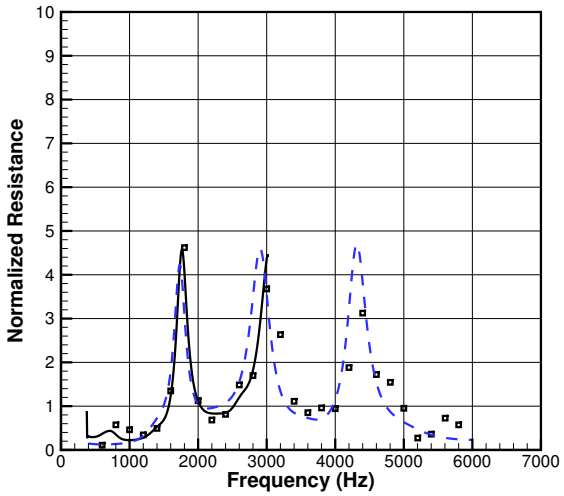

(a) 120 dB resistance

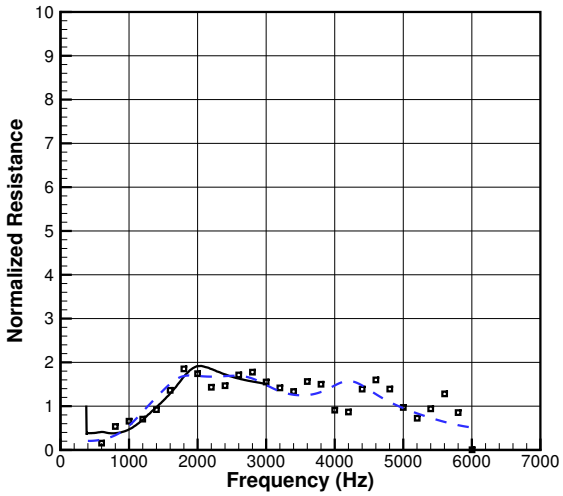

(b) 140 dB resistance

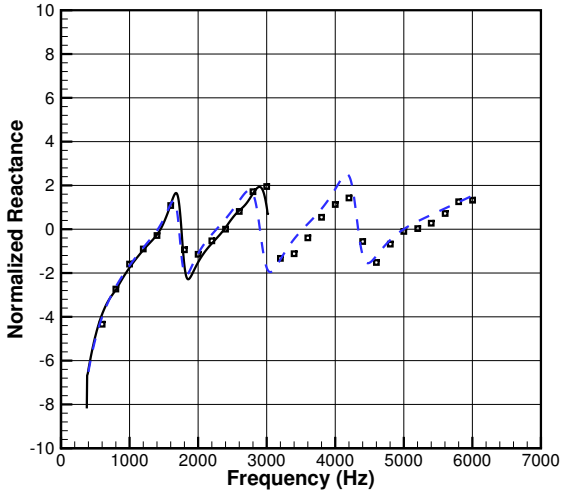

(c) 120 dB reactance

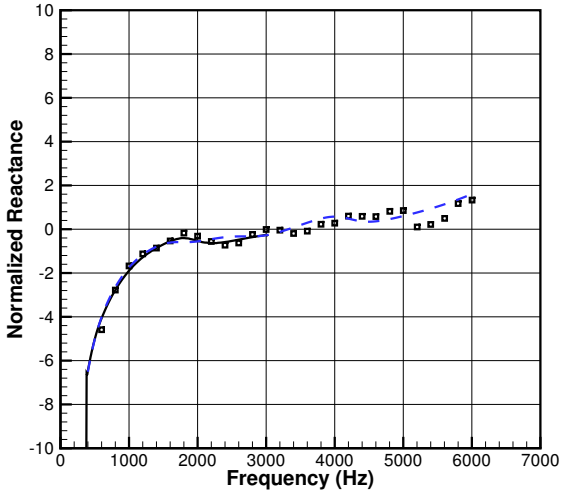

(d) 140 dB reactance

Fig. 7 Normalized impedance vs. frequency (Hz) for the P4 sample at SPL values of 120 and 140 dB. Black line is NIT data; Black squares are HIMIT data; Blue dashed line is prediction.

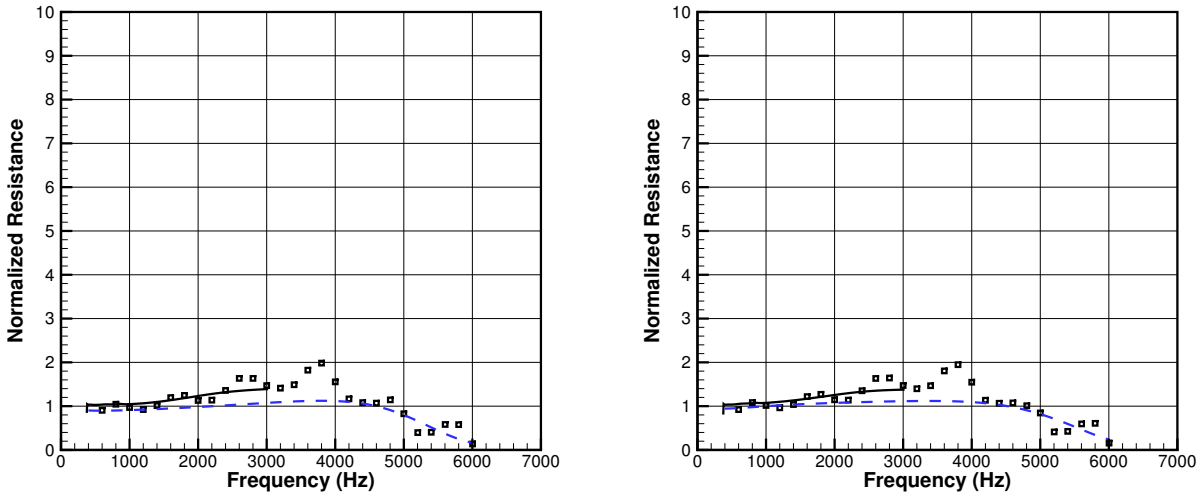

(a) 120 dB resistance

(b) 140 dB resistance

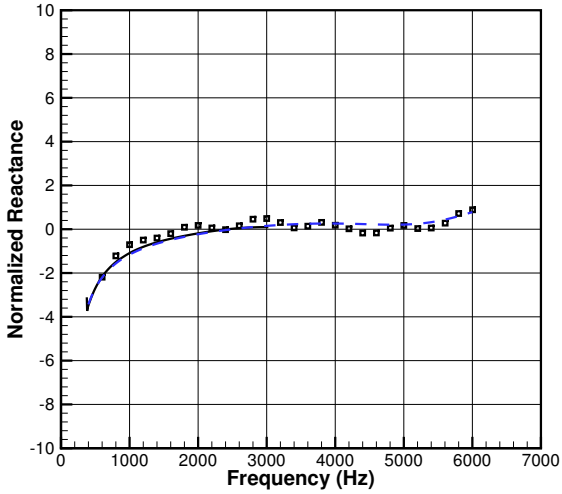

(c) 120 dB reactance

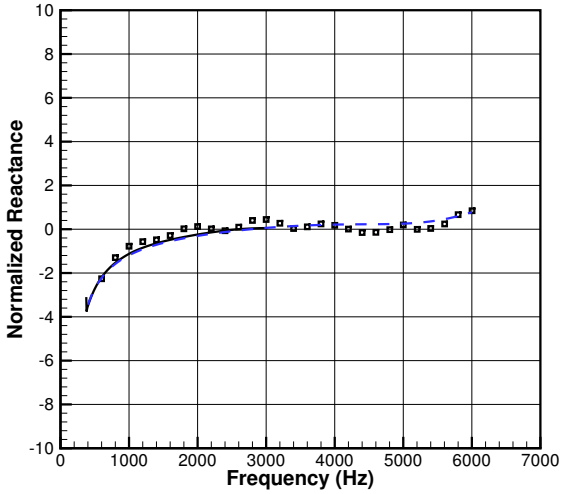

(d) 140 dB reactance

Fig. 8 Normalized impedance vs. frequency (Hz) for the T1 sample at SPL values of 120 and 140 dB. Black line is NIT data; Black squares are HIMIT data; Blue dashed line is prediction.

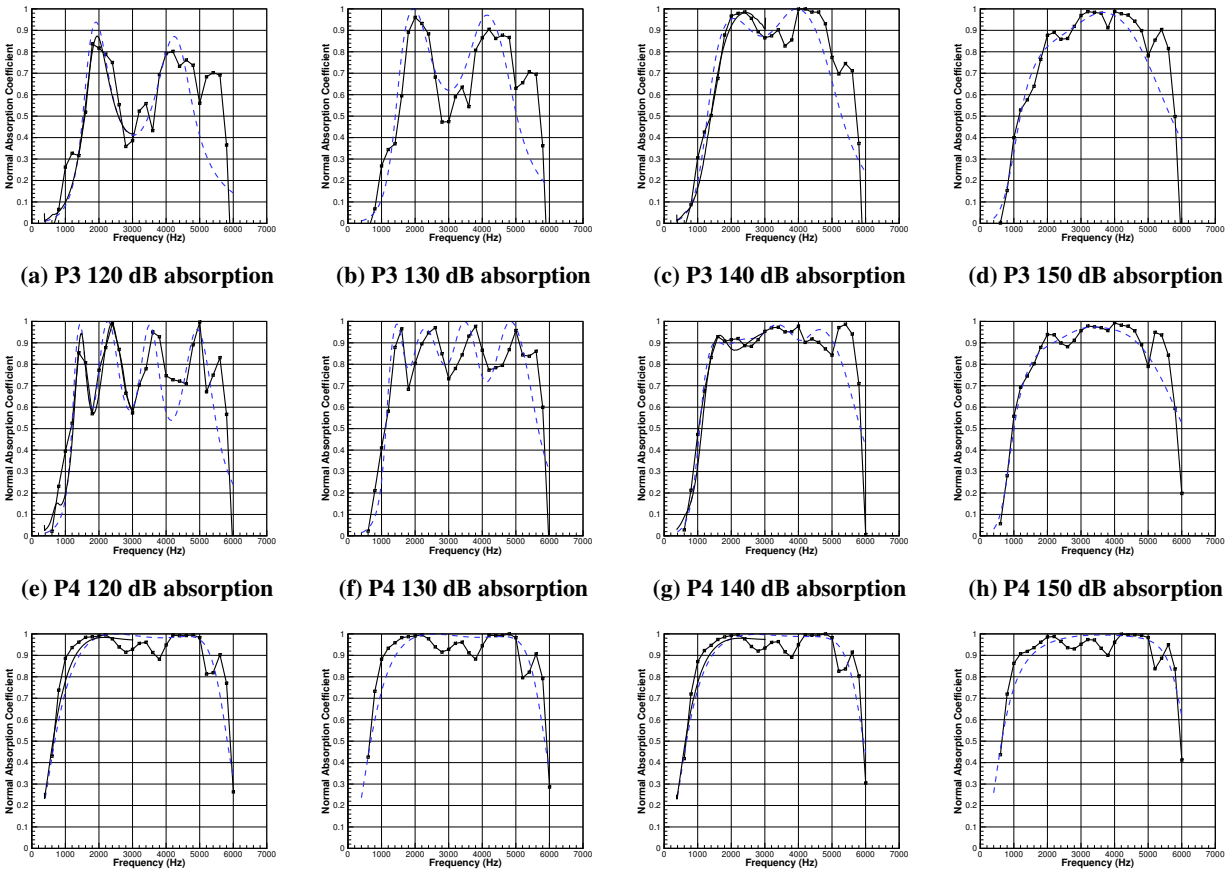

(a) P3 120 dB absorption (b) P3 130 dB absorption (c) P3 140 dB absorption (d) P3 150 dB absorption

(e) P4 120 dB absorption (f) P4 130 dB absorption (g) P4 140 dB absorption (h) P4 150 dB absorption

(i) T1 120 dB absorption (j) T1 130 dB absorption (k) T1 140 dB absorption (l) T1 150 dB absorption

Fig. 9 Normal incidence absorption coefficient vs. frequency (Hz) for all samples at SPL values of 120, 130, 140, and 150 dB. Black line is NIT data; Black line with squares is HIMIT data; Blue dashed line is prediction.

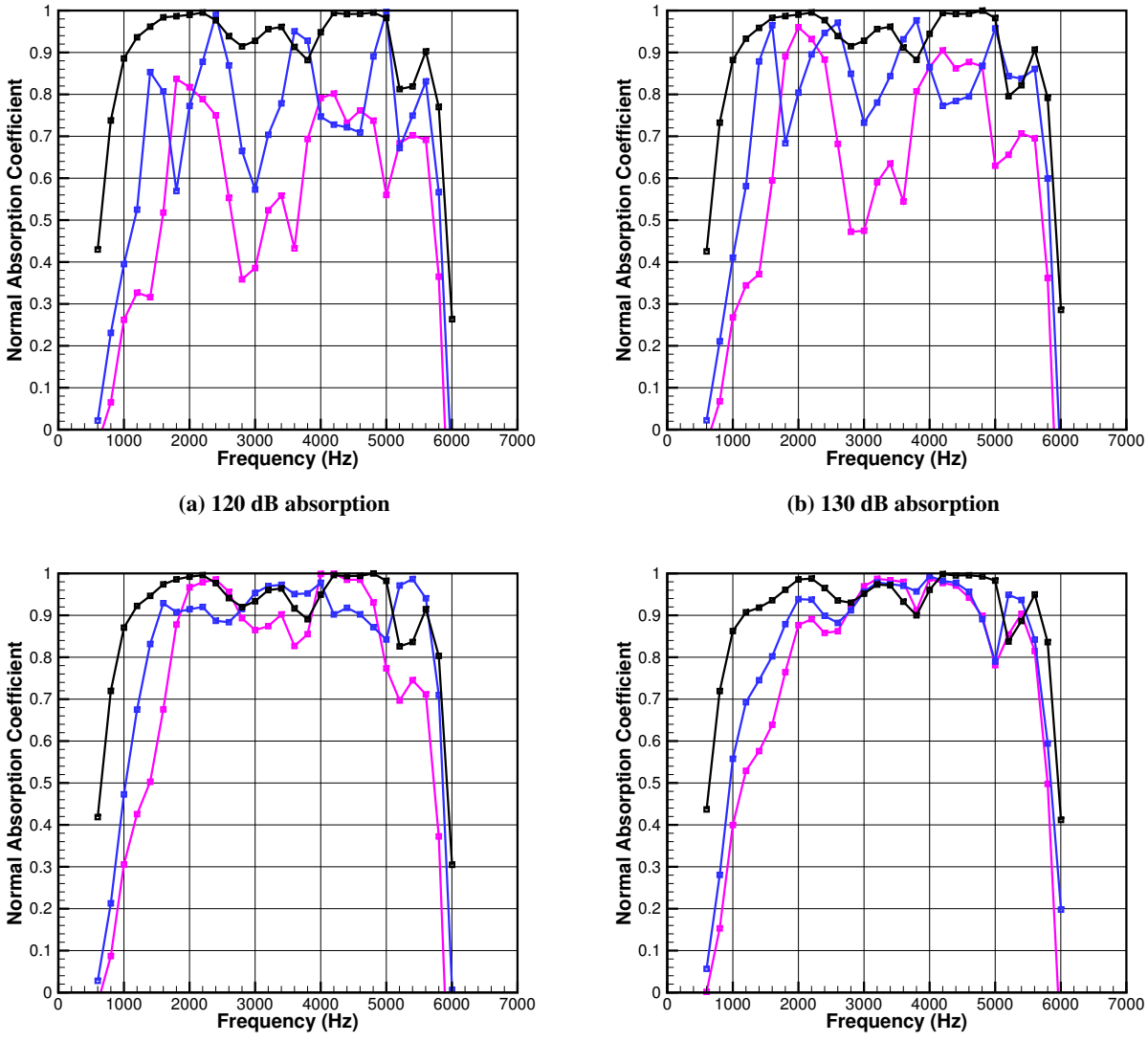

(a) 120 dB absorption

(b) 130 dB absorption

(c) 140 dB absorption

(d) 150 dB absorption

Fig. 10 Normal incidence absorption coefficient vs. frequency (Hz) for all samples at SPL values of 120, 130, 140, and 150 dB. Pink line with squares is the P3 liner; Blue line with squares is the P4 liner; Black line with squares is the T1 liner.

VIII. Summary and future work

Future aircraft require solutions for increased acoustic lining in unique areas of the aircraft where complex and high-curvature regions may exist. Liners fabricated using 3D-printing are a potential solution for addressing the treatment needs in these areas. To be as acoustically effective as modern engine acoustic liners, it is necessary to explore the possibility of 3D-printed 2DOF liners. An acoustic liner optimization tool was built using theory from the NASA Zwikker and Kosten Transmission Line (ZKTL) impedance prediction code. Candidate designs were established by optimizing liners in a normal incidence environment for an absorption coefficient of 1.0 over a wide range of frequencies and SPLs. Sample 3D-printed test articles, one constant and one variable chamber depth, were manufactured and tested along with a more traditional 2DOF liner with embedded mesh-caps. The basic findings are below:

- Impedance and absorption predictions generally show good agreement to test data, thereby validating the acoustic liner optimization tool.
- The 3D-printed, constant-chamber-depth 2DOF acoustic liner (P3), while demonstrating fairly broad absorption behavior, does not currently compare to the effectiveness of a traditional 2DOF liner with embedded mesh-caps (T1). This is primarily due to the constraint in 3D-printed hole size on the embedded perforate. It is also much more sensitive to the acoustic environment than the T1 liner.
- The 3D-printed, variable-chamber-depth 2DOF acoustic liner (P4) displays better absorption behavior than the P3 liner, although still not as good as the traditional 2DOF liner with embedded mesh-caps (T1). Adding more variable-depth channels to the design should produce results that more closely compare to the T1 liner.

Future work on this topic will include the following:

- Inclusion of embedded perforates within other novel 3D-printed concepts such as bent chambers
- Assessment of "hole clustering" on the embedded perforate to improve lower frequency performance [23]
- Enhancements to the acoustic liner optimization tool to better predict radiation impedance behavior of perforates, particularly the degradation due to SPL
- Inclusion of average SPL over the liner face in the prediction process of acoustic liners tested within HIMIT

Acknowledgments

The authors would like to acknowledge funding support provided by the Advanced Air Transport Technology Project of the NASA Advanced Air Vehicle Program. The authors would also like to thank Mr. Alonzo (Max) Reid for both developing the CAD and performing the quality assurance and post-processing on each sample. Finally, the authors wish to express thanks to Mr. Scott Haigler for acquiring data in the HIMIT.

References

[1] "HexWeb Aluminum Flex Core: Formable Aluminum Honeycomb, Product Data Sheet," 2017.

[2] Gautam, A., Celik, A., and Azarpeyvand, M., "On the acoustic performance of double degree of freedom helmholtz resonator based acoustic liners," *Journal of Applied Acoustics*, Vol. 191, 2022.

[3] Zwikker, C., and Kosten, C., *Sound Absorbing Materials*, Elsevier, Amsterdam, 1949.

[4] Tijdeman, H., "On the propagation of sound waves in cylindrical tubes," *Journal of Sound and Vibration*, Vol. 39, No. 1, March 1975, pp. 1–33.

[5] Parrott, T., and Jones, M., "Parallel Element Liner Impedances for Improved Absorption of Broadband Sound in Ducts," *Noise Control Engineering Journal*, Vol. 43, No. 6, 1995, pp. 183–195.

[6] Motsinger, R., and Kraft, R., "Design and Performance of Duct Acoustic Treatment: Aeroacoustics of Flight Vehicles; Chapter 14, Vol. 2: Noise Control," *NASA RP 1258*, August 1991.

[7] Yu, J., Ruiz, M., and Kwan, H., "Validation of Goodrich Perforate Liner Impedance Model Using NASA Langley Test Data," *AIAA Paper 2008-2930*, 2008.

[8] Kraft, R., Yu, J., and Kwan, H., "Acoustic Treatment Design Scaling Methods Volume 2: Advanced Treatment Impedance Models for High Frequency Ranges," *NASA CR-1999-209120*, 1999.

[9] Melling, T., "The Acoustic Impedance of Perforates at Medium and High Sound Pressure Levels," *Journal of Sound and Vibration*, Vol. 29, No. 1, 1973, pp. 1–65.

[10] Murray, P., Donnan, C., Richter, C., and Astley, J., "Development of a single degree of freedom micro-perforate impedance model under grazing flow and high SPL," *AIAA Paper 2016-2982*, 2016.

[11] Eversman, W., and Drouin, M., "Refinement of Impedance Models for Single and Two Degree of Freedom Linings Based on Grazing Flow Duct Predictions and Measurements," *AIAA Paper 2022-2966*, 2022.

[12] Betts, J., "Experiments and Impedance Modeling of Liners Including the Effect of Bias Flow," Ph.D. thesis, Virginia Polytechnic Institute and State University, 2000.

[13] Jones, M., Howerton, B., and Ayle, E., "Evaluation of Parallel-Element, Variable-Impedance, Broadband Acoustic Liner Concepts," *AIAA Paper 2012-2194*, 2012.

[14] Jones, M., and Nark, D., "Comparisons of Impedance Prediction Models for Perforate-over-Honeycomb Liners," *AIAA Paper 2023-3637*, 2023.

[15] Ingard, U., and Ising, H., "Acoustic Nonlinearity of an Orifice," *The Journal of the Acoustical Society of America*, Vol. 42, No. 1, 1967, pp. 6–17.

[16] Ingard, U., "On the Theory and Design of Acoustic Resonators," *The Journal of the Acoustical Society of America*, Vol. 25, No. 6, 1953, pp. 1037–1061.

[17] Johnson, S., "The NLopt nonlinear-optimization package," 2021. URL `http://github.com/stevengj/nlopt`.

[18] Powell, M., "The BOBYQA algorithm for bound constrained optimization without derivatives," *Department of Applied Mathematics and Theoretical Physics, Cambridge England, technical report NA2009/06*, 2009.

[19] "Protolabs: Manufacturing. Accelerated," 2000. URL `www.protolabs.com`.

[20] Jones, M., Carr, A., Nark, D., and Becker, L., "Implementation of the NASA High Intensity Modal Impedance Tube," *NASA TM-20220017773*, 2022.

[21] Solano, C., Jones, M., Carr, A., and Nark, D., "High Intensity Modal Impedance Tube Development at NASA Langley," *NASA TM-20230000292*, 2023.

[22] Jones, M., Watson, W., Nark, D., Howerton, B., and Brown, M., "A Review of Acoustic Liner Experimental Characterization at NASA Langley," *NASA TP-2020-220583*, 2020.

[23] Kreitzman, J., and Jones, M., "Investigation of the impedance characteristics of perforate sheet hole clustering over an array of uniform depth chambers," *AIAA Paper*, 2024 (submitted for publication).